The basic effect of cloud radiative effects on tropical sea-surface temperature variability

Ying Li* and David W. J. Thompson

Department of Atmospheric Science, Colorado State University, Fort Collins, Colorado, USA

Dirk Olonscheck

Max Planck Institute for Meteorology, Hamburg, Germany

**Corresponding author address:* Ying Li, Department of Atmospheric Science, Colorado State University, 3915 W. Laporte Ave. Fort Collins, CO 80521

E-mail: Ying.Li@colostate.edu

ABSTRACT

Cloud radiative effects (CREs) are known to play a central role in governing the long-term mean distribution of sea-surface temperatures (SSTs). Very recent work suggests that CREs may also play a role in governing the *variability* of SSTs, particularly in the context of the El Niño/Southern Oscillation. Here, the authors exploit numerical simulations with varying representations of CREs to demonstrate that coupling between CREs and the atmospheric circulation has a much more general and widespread effect on tropical climate than that indicated in previous work.

The results reveal that coupling between CREs and the atmospheric circulation leads to robust increases in SST variability on timescales longer than a month *throughout* the tropical oceans. It is argued that the increases in tropical SST variance derive primarily from the coupling between SSTs and shortwave CREs: Coupling increases the memory in shortwave CREs on hourly and daily timescales, and thus reddens the spectrum of shortwave CREs and increases their variance on timescales spanning weeks to decades. Coupling between SSTs and CREs does not noticeably affect the variance of SSTs in the extratropics, where the effects of CREs on the surface energy budget are much smaller than the effects of the turbulent heat fluxes. The results indicate the basic but critical role of CREs in governing climate variability throughout the tropics.

1. Introduction

An increasing body of literature suggests that cloud radiative effects (CRE) play a key role in governing not only the *mean* atmospheric circulation and its response to global warming, but also its *variability* across a range of spatial and temporal scales. The advent of various remotely-sensed cloud products such as those derived from the CloudSAT /CALIPSO (Stephens et al. 2002) satellites has provided unprecedented insight into the vertical structure of clouds in the long-term mean (Zhang et al. 2007; Su et al. 2011; Su and Jiang 2013; Li et al. 2014b), and into the signatures of large-scale climate variability in various cloud properties in both the extratropics (Li et al. 2014a; Wall and Hartmann 2015; Li and Thompson 2016) and tropics (Eguchi and Shiotani 2004; Masunaga et al. 2008; Chen and Genio 2009; Tromeur and Rossow 2010; Jiang et al. 2011; Riley et al. 2011; Yuan and Houze 2013; Crueger and Stevens 2015; Ma and Kuang 2011). Numerical experiments run with varying representations of CRE have revealed the central role of clouds in simulations of the mean tropospheric and stratospheric circulations (Fermepin and Bony 2014; Li et al. 2015, 2017; Harrop and Hartmann 2016; Watt-Meyer and Frierson 2017), and in the simulated atmospheric circulation response to climate change (Ceppi et al. 2012, 2014; Ceppi and Hartmann 2015; Voigt and Shaw 2015, 2016; Ceppi and Hartmann 2016; Fläschner et al. 2018; Li et al. 2019).

Two recent studies have argued that cloud radiative feedbacks also play an important role in governing the amplitude of climate variability, particularly in the context of the El Niño/Southern Oscillation (ENSO) (Rädel et al. 2016; Middlemas et al. 2019). The studies both exploit "locked-clouds" experiments, but they were run on different numerical models and use slightly different experiment frameworks. In both studies, the effects of CRE on the circulation are estimated by comparing output from 1) a control simulation where CRE are coupled to the atmospheric circulation and 2) a "locked-clouds" simulation where the CRE input into the model radiation code are decoupled from the atmospheric circulation. In the case of Middlemas et al. (2019), the CRE in the locked simulation were determined by repeating values of the CRE derived from a single, sample year from the control simulation. As such the CRE prescribed in the locked run have a similar diurnal and seasonal cycle to those found in the control run, but no interannual variability. In the case of Rädel et al. (2016), the CRE in the locked simulation were determined by randomizing the year assigned to each time step in the control output. The two studies yield slightly different results: Rädel et al. (2016) found that ENSO variability is enhanced across all timescales when CRE are coupled to the atmospheric circulation positive longwave cloud radiative feedbacks, whereas Middlemas et al. (2019) found that ENSO variability is only enhanced on timescales shorter than 6 years, but reduced on timescales longer than that due to negative shortwave cloud radiative feedbacks. Possible reasons for the different responses in the two simulations are differences in the model treatment of shortwave and longwave feedbacks (Lloyd et al. 2011, 2012; Bellenger et al. 2014) and - as noted below - differences in the locking methodology.

Here we argue that CREs play a much more basic role in governing the variance of SSTs than that indicated in previous studies. We demonstrate that coupling between CREs and the atmospheric circulation not only projects onto SSTs associated with the model ENSO, but that it also enhances the month-to-month variability of SSTs by a factor of 2–3 *throughout* the tropical oceans. It is suggested that the basic effect of coupling between clouds and the atmospheric circulation is to redden the spectrum of shortwave CRE, thus reducing its variance on daily and shorter timescales but increasing its variance on monthly and longer timescales. The increased variance of shortwave CRE on monthly timescales, in turn, leads to notable increases in the SST variance over the tropics (where surface temperature variability is dominated by the shortwave radiative flux), but not over the extratropics (where surface temperature variability is dominated by the turbulent heat fluxes). The basic effect of CREs on SSTs identified here is not realized in the locked simulations in Middlemas et al. (2019), since the prescribed CRE in those experiments correspond to annually-repeating values drawn a single year from the control, and thus have roughly the same autocorrelation as the CRE in the control. This is important, since the autocorrelation in CRE in the control is, in turn, due in part to the effects of coupling with the atmospheric circulation.

2. Locked-clouds simulations

As in Rädel et al. (2016) and Middlemas et al. (2019), the effects of CRE on the circulation are assessed by comparing output from 1) a control simulation where CRE are coupled to the atmospheric circulation and 2) a "locked-clouds" simulation where the CRE are prescribed and thus decoupled from the circulation.

The simulations were run on the latest version of the MPI model, the MPI-ESM1.2-LR, and with preindustrial forcing. The model has T63 ($\sim$200 km) horizontal resolution and 47 vertical layers in the atmosphere component (ECHAM6.3), and nominal 1.5° horizontal resolution and 40 vertical layers in the ocean component (MPIOM 1.6.3). The MPI-ESM1.2-LR is the baseline version used in the sixth Coupled Model Intercomparison Project (Eyring et al. 2016).

The locked simulations were performed in an analogous manner to that applied to an earlier version of the Max Planck Institute Earth System Model at low resolution (MPI-ESM1.0-LR), as described in Rädel et al. (2016). That is:

1. Key cloud parameters - including cloud fraction and cloud liquid/ice water content - were saved from a 250-year long control simulation at every two-hour radiation call.

2. The cloud parameters from the control run were scrambled by randomizing the year assigned to each time step, but not the hour or day. As such, the randomized cloud parameters have

the same long-term mean diurnal and seasonal cycles, have no memory from one time step to the next (e.g., output at 00Z01Jan is assigned a different year than output at 02Z01Jan, etc), and are decoupled from the circulation. As discussed below, the lack of autocorrelation in the cloud fields plays an important role in changing the low-frequency variance of the attendant CREs.

3. The scrambled cloud fields were then read into the radiation code of the locked-clouds simulation at every two-hour radiation call. The cloud locking method is only applied to the radiative transfer scheme; all other model components use internally simulated clouds.

The control and locked-clouds simulations are both 250-yrs in length, but the first 50 years of both simulations are discarded to account for the warming adjustment in the locked-clouds simulation.

Decoupling the cloud fields from the circulation leads to a weak warm bias in the locked-clouds simulations relative to the control run. A similar climate drift is found in other locked-clouds simulations, and is thought to arise from the small artificial radiative forcing that arises from the loss of spatio-temporal structure in clouds (Schneider et al. 1999; Langen et al. 2012; Mauritsen et al. 2013; Rädel et al. 2016; Middlemas et al. 2019). The focus of this study is on the variance of surface temperature and thus we expect the mean temperature bias should have no effect on the results shown here.

3. The influence of cloud radiative effects on tropical SST variability

We focus our analysis on a comparison of month-to-month variability in 1) the control simulation, where clouds are coupled to the circulation (hereafter referred to as the "interactive" clouds run) and 2) the "locked" clouds run, where clouds are decoupled from the circulation. The differences in climate variability between the interactive and locked clouds simulations derive entirely from the role of coupling between CRE and the circulation.

Figure 1a shows the variance of monthly-mean SST anomalies in the interactive-clouds run. Areas where the simulated SST variability is pronounced include 1) regions where upwelling is important, especially the equatorial Pacific; and 2) regions where ocean heat transport and atmospheric temperature advection are important, such as the western North Atlantic and North Pacific. Figure 1b shows the same results for the locked-clouds run. At first glance, the patterns of SST variance in the control interactive and locked clouds runs appear to differ only in the eastern tropical Pacific. But closer inspection of the results reveals marked differences *throughout* the tropical oceans.

Figure 1c shows the ratios of the SST variances in the interactive and locked clouds simulations. Values greater than one indicate regions where coupling between CRE and the circulation act to increase the variance in SSTs, and vice versa. Areas where the variance ratios are statistically significant at the 95% significance level based on the F-statistic are stippled. The most prominent ratios in Fig. 1c are found at tropical latitudes, where coupled CREs lead to increases in SST variance by a factor of 2–3 across the tropical Indian, Pacific and Atlantic oceans. The increases in variance over the tropical Pacific are consistent with the amplification of El Niño events found in Rädel et al. (2016) (and in Middlemas et al. (2019) on timescales less than $\sim$6 years). However, and importantly, similar increases in SST variance are found *throughout* the tropical oceans. As demonstrated in Appendix Fig. A1, the increases in tropical SST variance transcend the linear response to increasing SST variance in the eastern tropical Pacific (Schott et al. 2009; Xie and Carton 2004; Chang et al. 2006). In fact, as argued later, the bulk of the differences in tropical SST variance shown here arise not from the projection of CRE onto ENSO, but from a much more basic effect of CRE on surface temperatures.

The tropics-wide increases in SST variance are associated with a range of differences in various other tropical fields. The increases in SST variance lead to increases in the variance of upper tropospheric temperatures throughout the tropics (Fig. 2a), consistent with the facts that tropical atmospheric temperatures are strongly modulated by the SST field and closely follow the moist adiabatic lapse rate. They are associated with increases in the variances of convective precipitation (Fig. 2b), particularly over the tropical Pacific where the SST variance ratios are largest. And they are associated with increases in the variances of the upper tropospheric geopotential height field (Fig. 2c). The increases in the variance of upper tropospheric geopotential height project onto the structure of the model equatorial planetary waves, as evidenced by the close correspondence between 1) the equatorial troughs and ridges in the climatological-mean geopotential height field (black contours in Fig. 2d) and 2) the variance ratios in the eddy geopotential height field (shading in Fig. 2d).

4. Interpretation

Figure 1 reveals marked increases in SST variance throughout the tropics in simulations run with interactive cloud radiative effects. In this section, we quantify the physical factors that drive the increases in SST variance by diagnosing the attendant changes in the surface energy budget.

The energy budget for the surface mixed layer of the ocean can be expressed in monthly-mean anomaly form as:

$$C_o \frac{\partial T'}{\partial t} = Q'_{SW} + Q'_{LW} + Q'_{LH} + Q'_{SH} + Q'_{EK} + Q'_{geo}, \quad (1)$$

where primes denote monthly-mean anomalies (departures from the long-term mean seasonal cycle); T' is the anomalous temperature of the mixed layer (assumed proportional to the anomalous SST); C_o is the effective heat capacity of the mixed layer ($C_o = C_p \rho h$, in which ρ and C_p are the density and specific heat capacity at constant pressure of the seawater, h is the mixed layer depth);

and the Q' are the heatings due to anomalous surface shortwave radiative flux (Q'_{SW}), longwave radiative flux (Q'_{LW}), latent heat flux (Q'_{LH}), sensible heat flux (Q'_{SH}), advection by the Ekman flow (Q'_{EK}) and advection by the surface geostrophic flow (Q'_{geo}). Here $Q_{EK} = C_o \vec{V_{EK}} \cdot \nabla T$ and $Q_{geo} = C_o \vec{V_{geo}} \cdot \nabla T$, in which $\vec{V_{EK}}$ is the Ekman flow induced by the wind stress (τ) and $\vec{V_{geo}}$ is the geostrophic currents. We neglect vertical advection at the bottom of the mixed layer since outside of upwelling regions it plays a comparatively small role in the energy budget.

Following Yu and Boer (2006), Eq. 1 can be manipulated to yield an expression for the temperature variance by a) taking the centered difference of Eq. 1, b) squaring the result, and c) taking the time-mean. As reviewed in Methods, the above operation yields the following expression for the temperature variance:

$$\sigma_T^2 = G \cdot \sigma_\Sigma^2 \cdot e \tag{2}$$

where

- σ_T^2 is the variance of the SST field.
- $\sigma_\Sigma^2 = \sigma_{SW}^2 + \sigma_{LW}^2 + \sigma_{LH}^2 + \sigma_{SH}^2 + \sigma_{EK}^2 + \sigma_{geo}^2$ is the sum of the variances of the surface heat fluxes and ocean heat transport. Larger variances in the flux and transport terms lead to larger variance in the SST field, and vice versa.
- e includes the sum of the covariances between the heat flux terms (e.g., $e = 1 + \frac{2\Sigma(cov(Q_i,Q_j))}{\sigma_\Sigma^2}$, where $\Sigma(cov(Q_i,Q_j)) = cov(Q'_{SW},Q'_{LH}) + cov(Q'_{SW},Q'_{SH}) + cov(Q'_{SW},Q'_{EK}) + \cdots$). e may be viewed as an "efficiency factor" that measures the extent to which the variances in the flux and transport terms operate independently in modifying the SST variance (Yu and Boer 2006).
- $G = \frac{2(\Delta t)^2}{C_o^2(1-r_2)}$ may be viewed as a "transfer factor" that accounts for the effects on the temperature variance of the sampling timescale (Δt), the persistence (related to lag-2 autocorrelation r_2), and the effective heat capacity (C_o) (Yu and Boer 2006).

The left and middle columns in Fig. 3 explore the contributions of the individual terms in σ_{Σ}^{2} to the variances in monthly-mean SSTs in the interactive and locked simulations. The right column shows the percent contributions of the individual variances in the left column to the total variances in the interactive run. The primary features in the figures are the following:

1. The largest variances in the surface energy budget are found in association with the latent heat fluxes and are located over the subtropical and midlatitude oceans (panels g and h).

2. The variances in the ocean heat transport peak over regions where the climatological-mean SST gradients are largest (panels m and n) (Alexander 1992), and the variances in the sensible heat fluxes peak over the western sides of the Northern Hemisphere ocean basins (panels j and k), where there is commonly cold-advection from the continents upstream (Davis 1976; Miller 1992; Alexander 1992; Cayan 1992; Marshall et al. 2001; Alexander et al. 2002).

3. In the interactive simulation, the variances in the shortwave radiative fluxes have comparable amplitude throughout the globe (panel a). As evidenced in panel c and discussed further below, the shortwave radiative fluxes account for a comparatively large fraction of the total variance in the energy budget over the tropics since the latent heat fluxes are weakest there. The variances in the longwave radiative fluxes are relatively small and account for a small fraction of the surface flux variance everywhere (panels d and f).

4. By far the most pronounced differences between the interactive and locked simulations are found in the variances of the shortwave fluxes. The variances in monthly-mean shortwave heat fluxes are $\sim$200 W^4 m^{-4} throughout much of the globe when clouds are coupled to the circulation (panel a), but less than $\sim$20 W^4 m^{-4} in the locked simulation (panel b). As such the SW variance ratios are as large as $\sim$10 throughout much of the globe. As will be shown

later in Fig. 5, the reduced SW variance in the locked simulation is due to the whitening of CREs when clouds are decoupled from the circulation.

From Eq. 2, it follows that the ratios of temperature variance between the interactive and locked run can be diagnosed as:

$$\frac{\sigma^2_{T\ interactive}}{\sigma^2_{T\ locked}} = \frac{\sigma^2_{\Sigma\ interactive}}{\sigma^2_{\Sigma\ locked}} \cdot \frac{e_{interactive}}{e_{locked}} \cdot \frac{G_{interactive}}{G_{locked}} \tag{3}$$

Based on the results shown in Fig. 3, we assume 1) the variances associated with the shortwave and longwave radiative flux in the locked-clouds run are very small (Figs. 3b,e), 2) the variances associated other terms in the surface energy budget in the locked-clouds runs are approximately equal to those in the interactive run (compare Figs. 3g,h; Figs. 3j,k; Figs. 3m,n) and 3) the percentage contributions from the longwave radiative radiative flux to the total variance can be neglected (Fig. 3f). Based on the above, the first term in the RHS of Eq. 3 can be written as:

$$\frac{\sigma^2_{\Sigma\ interactive}}{\sigma^2_{\Sigma\ locked}} \approx \frac{\sigma^2_{\Sigma\ interactive}}{(\sigma^2_{LH} + \sigma^2_{SH} + \sigma^2_{EK} + \sigma^2_{geo})_{interactive}} \approx \frac{1}{1 - (\frac{\sigma^2_{SW}}{\sigma^2_{\Sigma}})_{interactive}}. \tag{4}$$

The simple scaling in Eq. 4 suggests that 1) the changes in the total variance of the surface energy flux between the interactive and locked-clouds simulations (LHS of Eq. 4) should peak over regions where 2) the shortwave cloud flux variance makes the largest contribution to the total energy flux variance in the interactive simulation (i.e., as shown in Fig. 3c).

Figure 4 quantifies the contributions of the various ratios in Eqs. 3–4 to the changes in temperature variance between the interactive and locked simulations. Figure 4a reproduces the ratios of the temperature variances from Fig. 1c (i.e., it shows the LHS of Eq. 3). Figure 4b shows the product of 1) the ratios of the surface flux and transport variances; 2) the "efficiency" (e); and 3) "transfer" (G) factors (i.e., it shows the RHS of Eq. 3). Figure 4c shows the first term only from the RHS of Eq. 3, which is equivalent to the sum of the results in the left columns in Fig. 3 ($\sigma^2_{\Sigma\ interactive}$)

divided by the sum of the results in the middle column ($\sigma^2_{\Sigma\ locked}$). Figure 4d shows the results of the scaling approximation from Eq. 4 (i.e., it highlights the key role of the SW radiative fluxes in the decomposition in Fig. 4c).

Comparing the results in Figs. 4a–c, it is clear that the ratios of SST variances between the interactive and locked simulations (Fig. 4a) can be quantitively reproduced by the decomposition given in Eq. 3 (Fig. 4b). The decomposition, in turn, is dominated by the first term on the RHS of Eq. 3. That is, the increases in SST variance in the interactive simulation arise primarily from the increases in the variance of the surface energy fluxes (Fig. 4c). The other two terms on the RHS of Eq. 3 (i.e., the "efficiency" and "transfer" factors) are dominated by 1) decreases in the covariances between the radiative fluxes in the locked run and 2) weak increases in SST persistence in the tropical and extratropical oceans in the interactive run (not shown). However, they play a relatively small role in the amplification of tropical SST variance between the interactive and locked simulations, as evidenced by the similarities between Figs. 4b and 4c. The fact that the differences in SST variance between the interactive and locked simulations peak at tropical latitudes (Fig. 4a) is consistent with the fact that the shortwave radiative fluxes play a more prominent role in the total variance of the surface energy fluxes at tropical latitudes than they do at extratropical latitudes (Fig. 4d; Eq. 4).

The key results in Figs. 3 and 4 are thus:

1. the preponderance of the differences in monthly-mean SST variance between the interactive and locked simulations (Fig. 1c) arise from the attendant differences in the monthly-mean shortwave radiative flux variances (Figs. 3a and 3b), and

2. the differences in monthly-mean SST variance peak in the tropics (Fig. 1c) since the variance in the shortwave radiative fluxes accounts for a relatively large fraction of the total variances in the surface energy budget there (Figs. 3c and 4d).

Why does the variance of the monthly-mean shortwave radiative flux increase when clouds are coupled to the atmospheric circulation? To understand this, we first consider the power spectrum of two standardized, random time series: 1) a white noise time series and 2) a red-noise time series with lag-one autocorrelation of $r1 = 0.9$. For the purpose of comparison to the numerical model output, the increment between time steps is defined as two-hours. By construction, both time series have the same variance: one. However, the white noise time series has larger variance than the red noise time series at periods shorter than $\sim$28 hours (i.e., 14 time steps), whereas the red noise time series has much larger variance than the white noise time series at all periods longer than $\sim$1 day (Fig. 5a). The cutoff period at which a standardized red noise time series exhibits larger variance than a standardized white noise time series ranges from 14 time steps (i.e., 28 hours in the case of data sampled every 2 hours) when $r1 = 0.9$ to 5 time steps (i.e., 10 hours) when $r1 = 0.1$ (Fig. 5b).

Now consider the time series of total cloud fraction at a sample tropical grid point from the control interactive model simulations sampled at two-hourly intervals. In the interactive simulation, the cloud fraction has memory from one time step to the next of roughly $r1 \approx 0.9$. However, in the locked simulation - by construction - the cloud fraction has no memory from one time step to the next ($r1 = 0$). The total variance of the cloud fraction time series is identical in both the interactive and locked simulations. However, as is the case for the idealized white and red noise time series, the differences in the variance of cloud fraction between the two simulations is a function of frequency. The variance of cloud fraction in the interactive simulation is less than the variance of cloud fraction in the locked simulation at periods less than ∼24 hours, but exceeds the variance of cloud fraction in the locked simulation at periods greater than ∼1 days (Fig. 5b).

Hence, the increases in the variances in shortwave radiative fluxes - and thus in SSTs - between the interactive and locked simulations arises from the reddening of the cloud field when it is coupled to the atmospheric circulation. *The basic effect of two-way coupling between clouds and the atmospheric circulation is to increase the variance of CRE on timescales longer than a few days.* The increased variances in shortwave CRE have largest effect on the variance in SSTs at tropical latitudes, where the shortwave radiative fluxes account for a prominent fraction of the total variance in the surface energy fluxes. They have only a weak effect on the variances in SSTs at extratropical latitudes, where the shortwave radiative fluxes play a small role in the total surface energy flux.

5. Concluding remarks

It has been long established that cloud radiative effects play a central role in determining Earth's mean climate. It is becoming increasingly clear that they also play a key role in Earth's climate variability across a range of timescales. In two recent studies, Rädel et al. (2016) and Middlemas et al. (2019) argue that the inclusion of coupling between the atmospheric circulation and clouds projects onto the variance of the El Niño/Southern Oscillation, primarily due to the projection of longwave or shortwave CRE onto ENSO physics. Here we argue that coupling between the atmospheric circulation and CRE leads to a much broader and more basic effect on the climate system: Cloud circulation coupling is theorized to lead to widespread increases in SST variance that span the tropical oceans (Fig. 1c) and arise from changes in the variance of shortwave CRE (Figs. 3 and 4). The increases in SST variance spanning frequency bands from weeks to years are apparent over all tropical ocean basins (Fig. 6), and are not simply a reflection of the remote response to ENSO variability (see Appendix and Fig. A1).

We hypothesize that the increases in tropical SST variance in the interactive simulation arise from the "reddening" of shortwave cloud radiative effects when clouds are coupled to the circulation. Coupling between the atmospheric circulation and clouds increases the memory in clouds on day-to-day timescales (e.g., the e-folding timescale of cloud fraction is $\sim$1–2 days in sample time series drawn from the interactive simulation; Fig. 5). The reddening of the cloud field due to the memory inherent in the large-scale atmospheric circulation leads to a reduction in the variance of cloud fraction on timescales less than a few days, but large increases in the variance of cloud fraction on timescales greater than a few days (Fig. 5). Decomposition of the surface energy budget (Eq. 3 and 4) reveals that it is the resulting increases in the variance of monthly-mean shortwave CRE that lead to the increases in SST variance when clouds are coupled to the circulation. The increases in SST variance are most clear in the tropics, where the shortwave heat fluxes account for the largest fraction of the total variance in the surface energy budget (Figs. 3c and 4d). They are less clear in the extratropics, where SST variability is dominated by the surface turbulent heat fluxes (Fig. 3i). The hypothesis accounts for the ubiquity of enhanced SST variability on timescales spanning weeks to decades and throughout the tropical oceans.

Large-scale variations in tropical SSTs provide a source of potential predictability for the climate system on seasonal, interannual and potentially decadal time scales. They are also linked to a range of surface climate impacts throughout the tropics and extratropics. The results shown here make clear that a notable component of tropical SST variability arises from cloud-circulation coupling. The implications of the results for climate impacts and predictability will be explored in a companion study.

Acknowledgment. We thank Thorsten Mauritsen for assistance with the numerical model output. We also thank ... (to be completed after review).

APPENDIX A

Decomposition of the factors that contribute to the variance in SST

Taking the centered difference of Eq. 1:

$$C_o \frac{T'(t+\Delta t) - T'(t-\Delta t)}{2\Delta t} = Q'_{SW} + Q'_{LW} + Q'_{LH} + Q'_{SH} + Q'_{EK} + Q'_{geo}, \tag{A1}$$

where Δt is 1 month.

Taking the square of Eq. A1 and the time average (denoted by overbar), the *lhs* of the resulting equation is approximately equal to

$$\begin{aligned} &\approx \frac{C_o^2}{2(\Delta t)^2}\left(\overline{T(t)'^2} - \overline{T'(t+\Delta t)T'(t-\Delta t)}\right) \\ &= \frac{C_o^2(1-r_2)}{2(\Delta t)^2}\sigma_T^2 \end{aligned} \tag{A2}$$

where σ_T^2 is the variance of the monthly-mean SST anomaly, and r_2 is lag-2 autocorrelation of SST anomaly computed as $\frac{\overline{T'(t+\Delta t)T'(t-\Delta t)}}{\overline{T(t)'^2}}$.

The *rhs* of the square and time average of Eq. A1 is equal to:

$$\sigma_\Sigma^2 + 2\Sigma(cov(Q_i, Q_j)), \tag{A3}$$

where σ_Σ^2 is the total variances of the six heat fluxes and transport related variances: $\sigma_\Sigma^2 = \sigma_{SW}^2 + \sigma_{LW}^2 + \sigma_{LH}^2 + \sigma_{SH}^2 + \sigma_{EK}^2 + \sigma_{geo}^2$; and $\Sigma(cov(Q_i, Q_j))$ is the summed covariances of the individual six components: $\Sigma(cov(Q'_i, Q'_j)) = cov(Q'_{SH}, Q'_{LH}) + cov(Q'_{SH}, Q'_{SH}) + cov(Q'_{SH}, Q'_{EK}) + \ldots$. Note that the variances and covariances terms involving the radiation fluxes are approximately zero in the locked-clouds simulation.

Thus the variance of the SST can be approximately estimated from Eqs. A2–A3 as:

$$\sigma_T^2 = \frac{2(\Delta t)^2}{C_o^2(1-r_2)}(\sigma_\Sigma^2 + 2\Sigma(cov(Q_i,Q_j))) \quad \text{(A4)}$$

$$= G \cdot \sigma_\Sigma^2 \cdot e \quad \text{(A5)}$$

where $G = \frac{2(\Delta t)^2}{C_o^2(1-r_2)}$, $e = 1 + \frac{2\Sigma(cov(Q_i,Q_j))}{\sigma_\Sigma^2}$.

References

Alexander, M. A., 1992: Midlatitude atmosphere-ocean interaction during El Niño. Part I: The North Pacific Ocean. *J. Climate*, **5**, 944–958.

Alexander, M. A., I. Bladé, M. Newman, J. R. Lanzante, N.-C. Lau, and J. D. Scott, 2002: The atmospheric bridge: Influence of ENSO teleconnnections on air-sea interaction over the global oceans. *J. Climate*, **15**, 2205–2231.

Bellenger, H., E. Guilyardi, J. Leloup, M. Lengaigne, and J. Vialard, 2014: ENSO representation in climate models: from CMIP3 to CMIP5. *Clim. Dynam.*, **42**, 1999–2018, doi: 10.1007/s00382-013-1783-z.

Cayan, D. R., 1992: Latent and sensible heat flux anomalies over the northern oceans: driving the sea temperature. *J. Phys. Oceanogr.*, **22**, 859–881.

Ceppi, P., and D. L. Hartmann, 2015: Connections between clouds, radiation, and midlatitude dynamics: a review. *Curr. Clim. Change Rep.*, doi:10.1007/s4061-015-0010-x.

Ceppi, P., and D. L. Hartmann, 2016: Clouds and the atmospheric circulation response to warming. *J. Climate*, **29**, 783–799, doi:10.1002/2014GL060043.

Ceppi, P., Y.-T. Hwang, D. M. W. Frierson, and D. L. Hartmann, 2012: Southern Hemisphere jet latitude biases in CMIP5 models linked to shortwave cloud forcing. *Geophys. Res. Lett.*, **39**, L19 708, doi:10.1029/2012GL053115.

Ceppi, P., M. D. Zelinka, and D. L. Hartmann, 2014: The response of the Southern Hemispheric eddy-driven jet to future changes in shortwave radiation in CMIP5. *Geophys. Res. Lett.*, **41**, 3244–3250, doi:10.1002/2014GL060043.

Chang, P., and Coauthors, 2006: Climate fluctuations of tropical coupled systems: the role of ocean dynamic. *J. Climate*, **19**, 51225174.

Chen, Y., and A. D. D. Genio, 2009: Evaluation of tropical cloud regimes in observations and a general circulation mode. *Clim. Dynam.*, **32**, 355–369, doi:10.1007/S00382-008-0386-6.

Crueger, T., and B. Stevens, 2015: The effect of atmospheric radiative heating by clouds on the Madden-Julian Oscillation. *J. Adv. Model. Earth Syst*, doi:10.1002/2015MS000434.

Davis, R. E., 1976: Predictability of sea surface temperature and sea level pressure anomalies over the North Pacific Ocean. *J. Phys. Oceanogr.*, **6**, 249–266.

Eguchi, N., and M. Shiotani, 2004: Intraseasonal variations of water vapor and cirrus clouds in the tropical upper troposphere. *J. Geophys. Res.*, **109**, D12 106, doi:10.1029/2003JD004314.

Eyring, V., S. Bony, G. A. Meehl, C. A. Senior, B. Stevens, R. J. Stouffer, and K. E. Taylor, 2016: Overview of the Coupled Model Intercomparison Project Phase 6 (CMIP6). *Geosci. Model Dev.*, **9**, 1937–1958, doi:10.5194/gmd-9-1937-2016.

Fermepin, S., and S. Bony, 2014: Influence of low-cloud radiative effects on tropical circulation and precipitation. *J. Adv. Model. Earth Syst*, **06**, doi:10.1002/2013MS000288.

Fläschner, D., T. Mauritsen, B. Stevens, and S. Bony, 2018: The signature of shallow circulations, not cloud radiative effects, in the spatial distribution of tropical precipitation. *J. Climate*, 9489–9505, doi:10.1175/JCLI-D-18-0230.1.

Harrop, B. E., and D. L. Hartmann, 2016: The role of cloud radiative heating in determining the location of the ITCZ in aquaplanet simulations. *J. Climate*, **29**, 2741–2763, doi:10.1175/JCLI-D-15-0521.1.

Jiang, X., D. E. Waliser, J.-L. Li, and C. Woods, 2011: Vertical structures of cloud water associated with the boreal summer intraseasonal oscillation based on CloudSat observations and ERA-Interim reanalysis. *Clim. Dynam.*, **10**, doi:10.1007/s00382-010-0853-8.

Langen, P. L., R. G. Graversen, and T. Mauritsen, 2012: Separation of contributions from radiative feedbacks to polar amplification on an aquaplanet. *J. Climate*, **25**, 3010–3024, doi:10.1175/JCLI-D-11-00246.1.

Li, Y., and D. W. J. Thompson, 2016: Observed signatures of the barotropic and baroclinic annular modes in cloud vertical structure and cloud radiative effects. *J. Climate*, **29**, 4723–4740.

Li, Y., D. W. J. Thompson, and S. Bony, 2015: The influence of atmospheric cloud radiative effects on the large-scale atmospheric circulation. *J. Climate*, **28**, 7263–7278, doi:10.1175/JCLI-D-14-00825.1.

Li, Y., D. W. J. Thompson, S. Bony, and T. M. Merlis, 2019: Thermodynamic control on the poleward shift of the extratropical jet in climate change simulations. *J. Climate*, **32**, 917–934.

Li, Y., D. W. J. Thompson, and Y. Huang, 2017: The influence of atmospheric cloud radiative effects on the large-scale stratospheric circulation. *J. Climate*, **30**, 5621–5635, doi:10.1175/JCLI-D-16-0643.1.

Li, Y., D. W. J. Thompson, Y. Huang, and M. Zhang, 2014a: Observed linkages between the Northern Annular Mode/North Atlantic Oscillation, cloud incidence, and cloud radiative forcing. *Geophys. Res. Lett.*, **41**, 1681–1688, doi:10.1002/2013GL059113.

Li, Y., D. W. J. Thompson, G. L. Stephens, and S. Bony, 2014b: A global survey of the linkages between cloud vertical structure and large-scale climate. *J. Geophys. Res.*, **119**, 3770–3792, doi:10.1002/2013JD020669.

Lloyd, J., E. Guilyardi, and H. Weller, 2011: The role of atmosphere feedbacks during ENSO in the CMIP3 models. Part II: using AMIP runs to understand the heat flux feedback mechanisms. *Clim. Dynam.*, **37**, 1271–1292, doi:10.1007/s00382-010-0895-y.

Lloyd, J., E. Guilyardi, and H. Weller, 2012: The role of atmosphere feedbacks during ENSO in the CMIP3 Models. Part III: The shortwave flux feedback. *J. Climate*, **25**, 4275–4293, doi: 10.1175/JCLI-D-11-00178.1.

Ma, D., and Z. Kuang, 2011: Modulation of radiative heating by the Madden-Julian Oscillation and convectively coupled Kelvin Waves as observed by CloudSat. *Geophys. Res. Lett.*, **38**, L21 813.

Marshall, J., H. Johnson, and J. Goodman, 2001: A study of the interaction of the North Atlantic Oscillation with ocean circulation. *J. Climate*, **14**, 1399–1421.

Masunaga, H., M. Satoh, and H. Miura, 2008: A joint satellite and global cloud-resolving model analysis of a Madden-Julian Oscillation event: Model diagnosis. *J. Geophys. Res.*, **113**, D17 210, doi:10.1029/2008JD009986.

Mauritsen, T., R. G. Graversen, D. Klocke, P. L. Langen, B. Stevens, and L. Tomassini, 2013: Climate feedback efficiency and synergy. *Clim. Dynam.*, **41**, 2539–2554, doi:10.1007/s00382-013-1808-7.

Middlemas, E. A., A. C. Clement, B. Medeiros, and B. Kirtman, 2019: Cloud radiative feedbacks and El Niño Southern Oscillation. *J. Climate*, revised.

Miller, A. J., 1992: Large-scale ocean-atmosphere interactions in a simplified coupled model of the midlatitude wintertime circulation. *J. Atmos. Sci.*, **49**, 273–286.

Rädel, G., T. Mauritsen, B. Stevens, D. Dommenget, D. Dommenget, D. Matei, K. Bellomo, and A. Clement, 2016: Amplification of El Niño by cloud longwave coupling to atmospheric circulation. Nature Geoscience. *Nature Geosci.*, **9**, 106–110.

Riley, E. M., B. E. Mapes, and S. N. Tulich, 2011: Clouds Associated with the MaddenJulian Oscillation: A New Perspective from CloudSat. *J. Atmos. Sci.*, **68**, 3032–3051, doi:10.1175/JAS-D-11-030.1.

Schneider, E. K., B. P. Kirtman, and R. S. Lindzen, 1999: Tropospheric water vapor and climate sensitivity. *J. Atmos. Sci.*, **56**, 1649–1658.

Schott, F. A., S.-P. Xie, and J. P. McCreary, 2009: Indian Ocean circulation and climate variability. *Rev. Geophys.*, **47**, RG1002, doi:10.1029/2007RG000245.

Stephens, G., and Coauthors, 2002: The CloudSat mission and the A-train: A new dimension of space-based observations of clouds and precipitation. *Bull. Amer. Meteor. Soc.*, **83**, 1771–1790, doi:10.1175/BAMS-83-12-1771.

Su, H., and J. H. Jiang, 2013: Tropical clouds and circulation changes during the 2006-07 and 2009-10 El Niños. *J. Climate*, **26**, 399–413, doi:10.1175/JCLI-D-12-00152.1.

Su, H., J. H. Jiang, J. Teixeira, A. Gettelman, X. Huang, G. Stephens, D. Vane, and V. S. Perun, 2011: Comparison of regime-sorted tropical cloud profiles observed by CloudSat with GEOS5 analyses and two general circulation model simulations. *J. Geophys. Res.*, **116**, D09 104, doi:10.1029/2010JD014971.

Tromeur, E., and W. B. Rossow, 2010: Interaction of tropical deep convection with the large-scale circulation in the MJO. *J. Climate*, **23**, 1837–1853, doi:10.1175/2009JCLI3240.1.

Voigt, A., and T. A. Shaw, 2015: Radiative changes of clouds and water vapor shape circulation response to global warming. *Nature Geosci.*, **8**, 102106, doi:10.1038/ngeo2345.

Voigt, A., and T. A. Shaw, 2016: Impact of regional atmospheric cloud radiative changes on shifts of the extratropical jet stream in response to global warming. *J. Climate*, **29**, 8399–8421, doi:10.1175/JCLI-D-16-0140.1.

Wall, C. J., and D. L. Hartmann, 2015: On the influence of poleward jet shift on Shortwave cloud feedback in GCMs. *J. Adv. Model. Earth Syst*, **07**, doi:10.1002/2015MS000520.

Watt-Meyer, O., and D. M. W. Frierson, 2017: Local and emote impacts of atmospheric cloud radiative effects onto the eddy-driven jet. *Geophys. Res. Lett.*, **44**, 10 036–10 044, doi:10.1002/2017GL074901.

Xie, S.-P., and J. A. Carton, 2004: Tropical atlantic variability: patterns, mechanisms, and impacts. *Earth Climate: The Ocean-Atmosphere Interaction*, C. Wang, S.-P. Xie, and J. A. Carton, Eds., Am. Geophys. Union, Washington DC, 121–142.

Yu, B., and G. J. Boer, 2006: The variance of sea surface temperature and projected changes with global warming. *Clim. Dynam.*, **26**, 801–821, doi:10.1007/s00382-006-0117-9.

Yuan, J., and R. A. Houze, 2013: Deep convective systems observed by A-Train in the tropical Indo-Pacific region affected by the MJO. *J. Atmos. Sci.*, **70**, 456–486, doi:10.1175/JAS-D-12-057.1.

Zhang, Y., S. Klein, G. G. Mace, and J. Boyl, 2007: Cluster analysis of tropical clouds using CloudSat data. *Geophys. Res. Lett.*, **34**, L12 813, doi:10.1029/2007GL029336.

LIST OF FIGURES

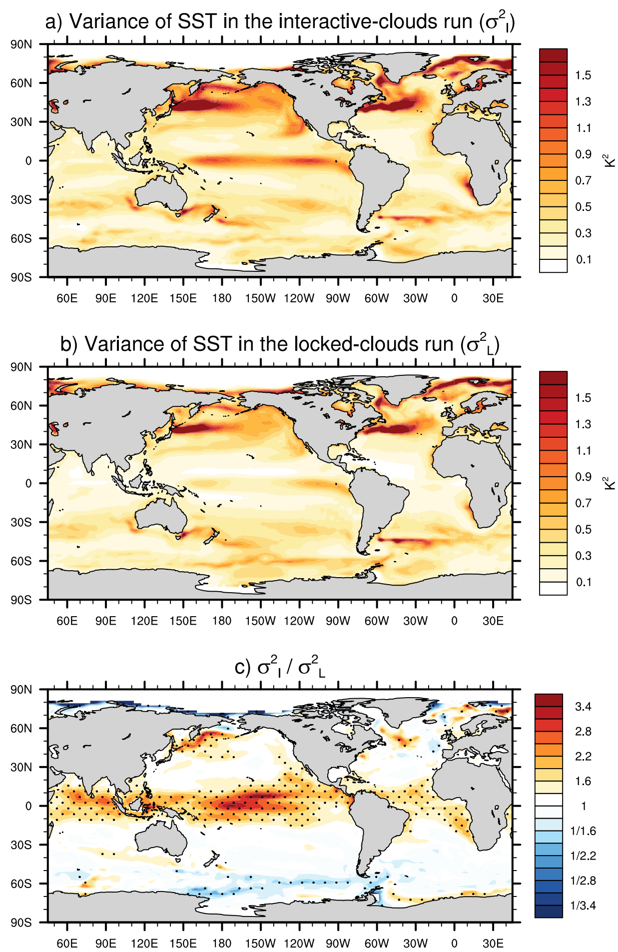

FIG. 1. The effect of interactive clouds on SST variance. (a) Variances of monthly-mean SST anomalies from the 200-yr interactive-clouds run. (b) Variances of monthly-mean SST anomalies from the 200-yr locked-clouds run. (c) Ratio of the variances between the interactive and locked runs. Ratios >1 indicate larger variability in the interactive run, and vice versa. Stippling indicates regions where the ratios are significant at the 95% level. Regions where the SST variance in (a) is less than 0.01 K^2 are masked when calculating the ratios in (c).

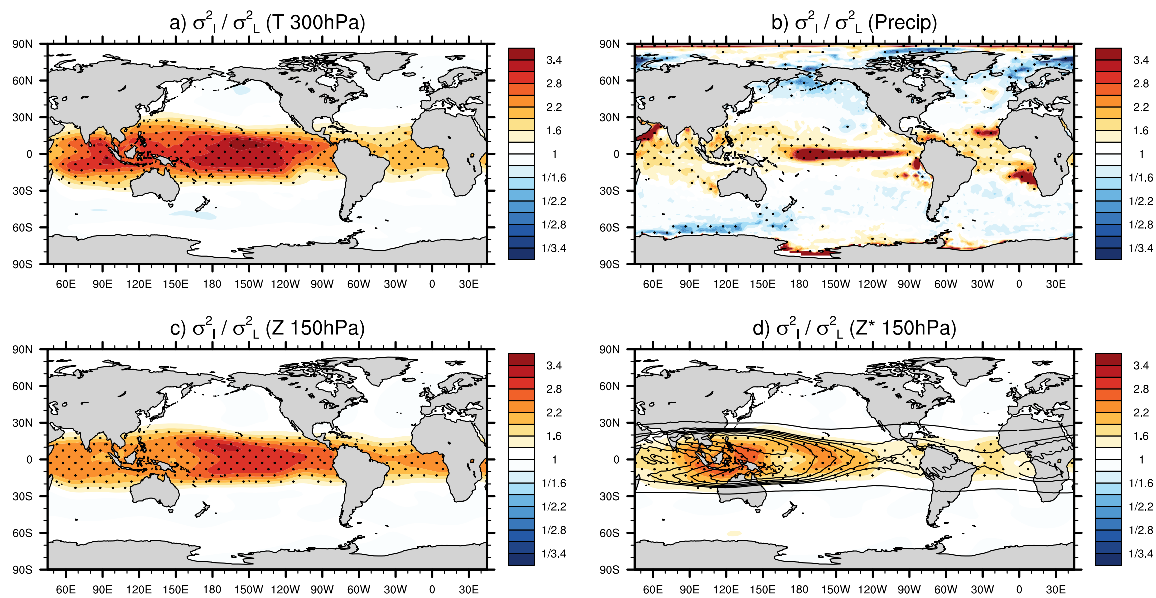

FIG. 2. The effects of interactive clouds on tropical climate. Ratio of the variances between the interactive and locked runs of (a) atmospheric temperature at 300 hPa, (b) convective precipitation, (c) geopotential height at 150 hPa, and (d) eddy geopotential height at 150 hPa. The black contours superimposed on panel d denote the long-term geopotential height at 150 hPa (contour interval: 14000, 14100, 14110, 14120, 14130 m...). Results are based on monthly-mean anomalies.

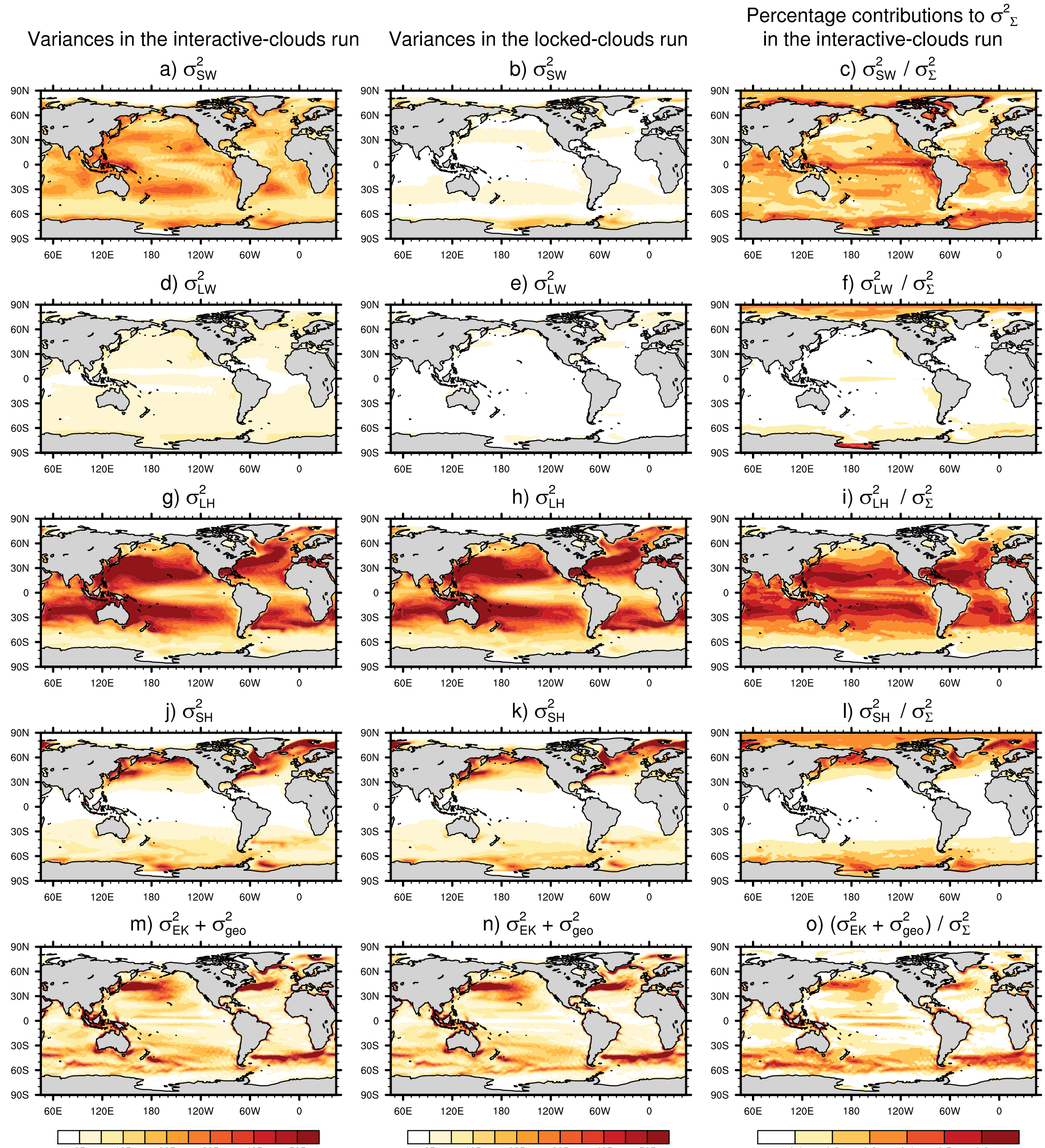

FIG. 3. Variances in the surface energy fluxes. (a, b) surface shortwave radiative flux, (d, e) longwave radiative fluxes, (g, h) latent heat flux, (j, k) sensible heat fluxes, (m, n) heat advection by the meridional Ekman and geostrophic current. Results for (left column) the 200-yr interactive-clouds simulation and (middle column) the 200-yr locked-clouds simulation. The right column is the percentage contribution of each terms to the total variance in the interactive-clouds simulation. Results are based on monthly-mean anomalies.

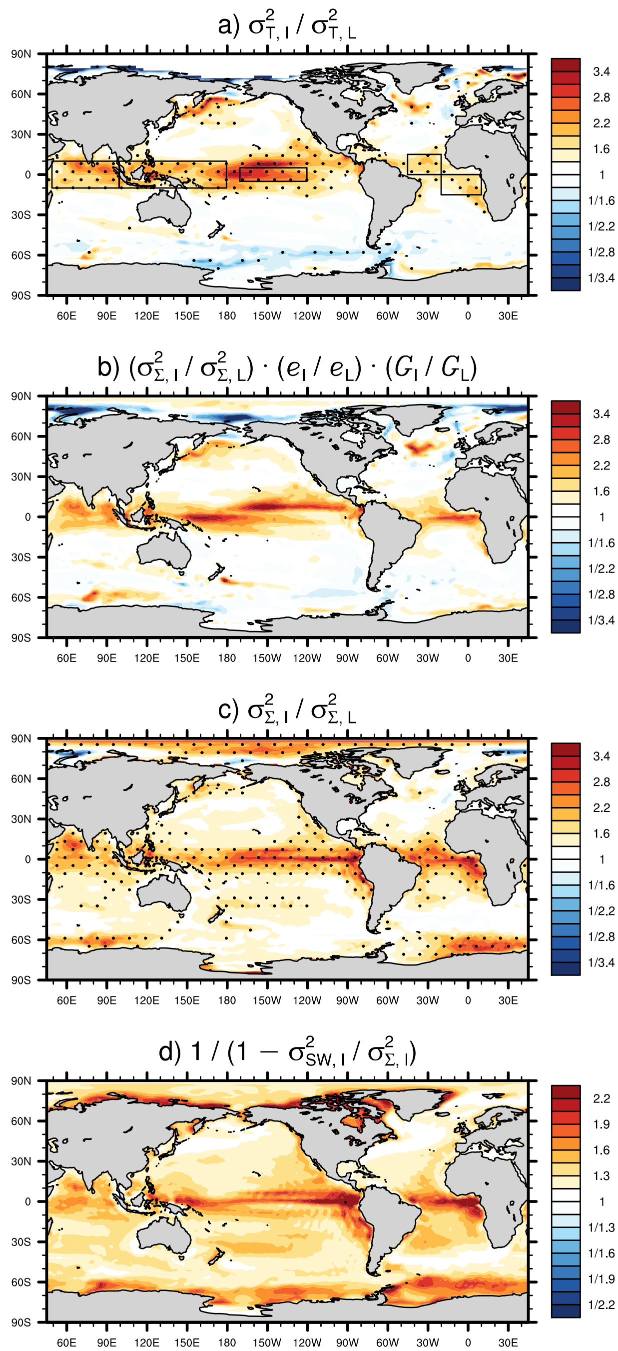

FIG. 4. Identifying the physical factors responsible for the increases in SST variance. (a) The ratios of the surface temperature variance between the interactive and locked simulations (reproduced from Fig. 1c). (b) The product of all three terms on the rhs of Eq. 3. (c) The contribution of the ratios in the sums of the surface fluxes (the first term on the rhs of Eq. 3). (d) The results of the approximation in Eq. 4, which highlights the dominant role of the SW radiative fluxes in the ratios shown in panel c (see text for details). Results are based on monthly-mean anomalies. Note that the color scales are different in panel (d) and other panels. The black boxes in (a) are the regions used for calculating the power spectra of the area averaged SST anomalies in Fig. 6.

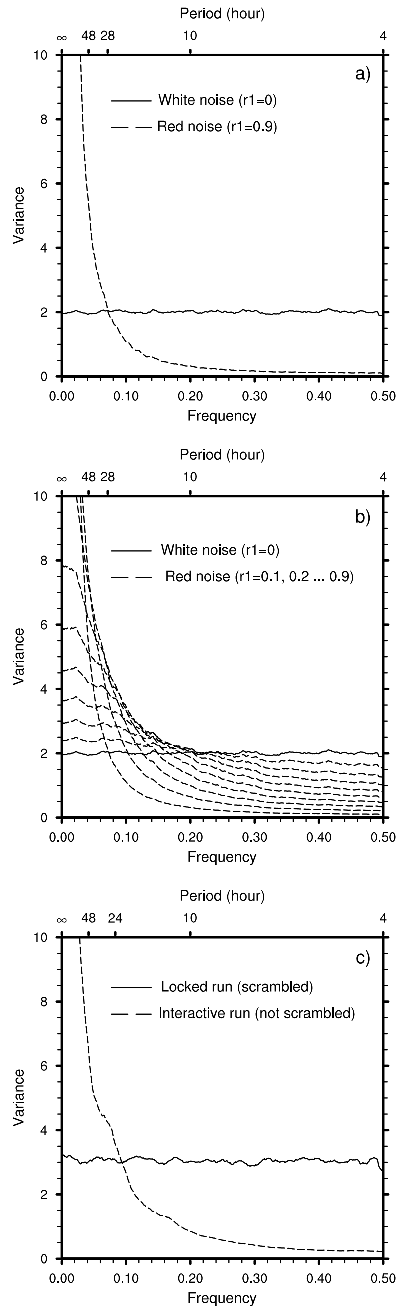

FIG. 5. The importance of persistence in the variance of cloud fraction. (a) Power spectra for a randomly generated red noise time series with lag-one autocorrelation of $r1 = 0.9$ (dashed line) and a white noise time series with $r1 = 0$ (solid line). (b) Same as (a), but for power spectra for a randomly generated red noise time series with lag-one autocorrelation ranging from $r1 = 0.1$ to $r1 = 0.9$ (dashed lines) and a white noise time series with $r1 = 0$ (solid line). (c) Power spectra for time series of cloud fraction at sample tropical grid point (0°, 180°) used in the interactive-clouds run (dashed line) and the locked-clouds run (solid). The cloud fraction time series are 50-yr long sampled at two-hourly intervals. The randomly generated time series used to construct the top panel are the same length as the cloud fraction time series.

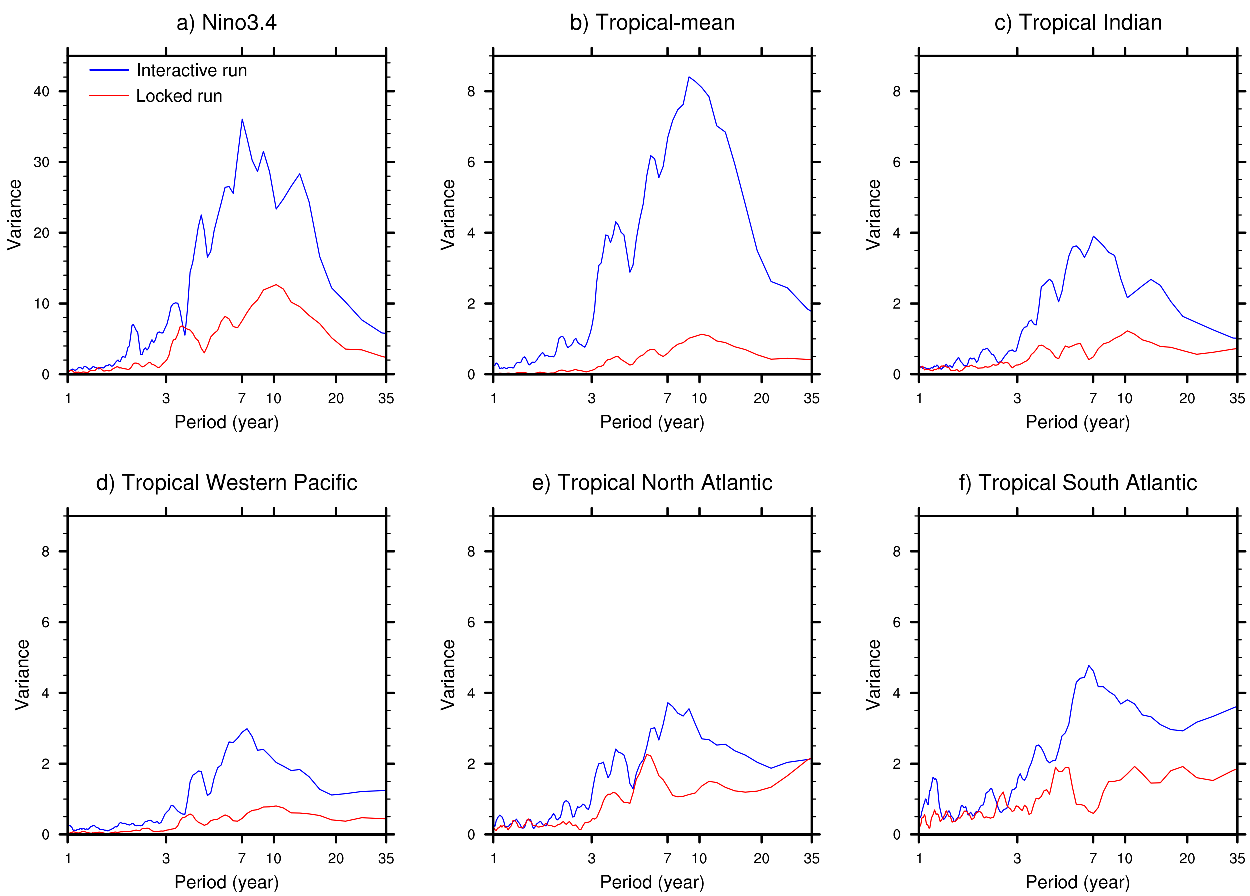

FIG. 6. Power spectra of SST anomaly time series for indicated regions. Power spectra of SST anomaly time series averaged over (a) Niño 3.4, (b) entire tropics (15°S–15°N), (c) tropical Indian ocean (10°S–10°N, 50°–100°E), (d) tropical western Pacific (10°S–10°N, 100°E–180°), (e) tropical north Atlantic (0°–15°N, 315°–340°E), and (f) tropical south Atlantic (15°S–0, 20°W–10°E). Results for the interactive-cloud simulation are indicated by the red lines, and for the locked-cloud simulation are indicated by the blue lines. Regions are indicated by the black boxes in Fig. 4.

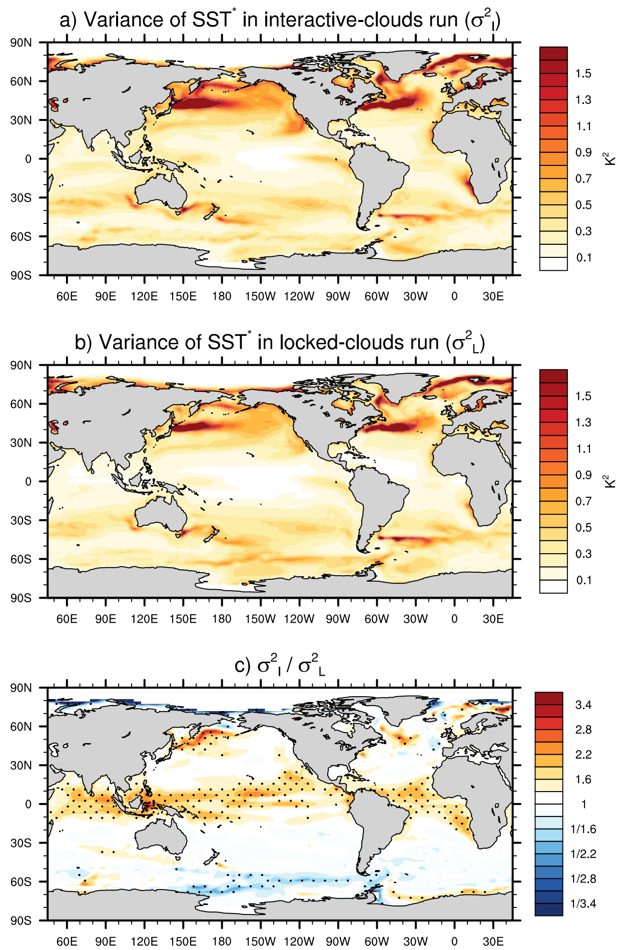

Fig. A1. SST variances in the interactive and locked simulation after linearly removing the effects of ENSO from the data. Same as Fig. 1, but for results after linearly regressing the Niñio3.4 index (SSTs averaged over 5°N–5°S, 170°W–120°W) from the SST data at all grid points. The regression is based on contemporaneous values of the SST field and the ENSO index; similar results are derived after lagging the SST field by three months (not shown).